Spontaneous profile self-organization in a simple realization of drift-wave turbulence

L. Cui, A. Ashourvan, S. C. Thakur, R. Hong, P. H. Diamond, and G. R. Tynan

Citation: Physics of Plasmas **23**, 055704 (2016); doi: 10.1063/1.4944819
View online: http://dx.doi.org/10.1063/1.4944819
View Table of Contents: http://scitation.aip.org/content/aip/journal/pop/23/5?ver=pdfcov
Published by the AIP Publishing

Spontaneous profile self-organization in a simple realization of drift-wave turbulence

L. Cui,[1,a)] A. Ashourvan,[1,2] S. C. Thakur,[1] R. Hong,[1] P. H. Diamond,[1,2] and G. R. Tynan[1]
[1]*Center for Energy Research, University of California San Diego, La Jolla, California 92093, USA*
[2]*Center for Astrophysics and Space Sciences (CASS) and Department of Physics, University of California San Diego, La Jolla, California 92093, USA*

(Received 30 November 2015; accepted 5 February 2016; published online 25 March 2016)

We report the observation of a transport bifurcation that occurs by spontaneous self-organization of a drift-wave and shear flow system in a linear plasma device. As we increase the magnetic field above a threshold ($B_{Cr} = 1200$ G), a global transition occurs, with steepening of mean density and ion pressure profiles, onset of strong E × B shearing, a reduction of turbulence, and improved turbulent radial particle transport. An abrupt transition appears in the graph of turbulent particle flux versus density gradient. Hysteresis in the density gradient further confirms this transport bifurcation. The total Reynolds work on the flow sharply increases above threshold. This correlates with the increase of density steepness, which suggests the Reynolds stress-driven flow that plays an essential role in density steepening and transport bifurcation. A change in turbulence feature from drift waves (DWs) to a mix of DWs and ion temperature gradients also coincides with the transport bifurcation. Interesting phenomena related to the transport bifurcation are also reported; a local inward particle flux, the co-existence of ion and electron features, and a self-sustained axial flow absent momentum input. © *2016 AIP Publishing LLC*. [http://dx.doi.org/10.1063/1.4944819]

I. INTRODUCTION

In magnetically confined plasmas, experiments on low-mode (L-mode) to improved confinement-mode (H-mode) transitions (L-H transitions) have shown that in order to enter H-mode, a threshold power input, P_{LH}, must be exceeded. At that point, a bifurcation to an enhanced confinement occurs. These enhanced confinement states are characterized by steepened profile gradients and (often) strongly sheared radial electric fields. When the heating power is reduced, the threshold for the back transition from H-mode to L-mode (the H-L back transition) occurs at a different power $P_{HL} < P_{LH}$. This bifurcation threshold hysteresis in the macroscopic transition condition is manifested in a *nonlinear relationship* between the heat flux and the plasma gradients.[1] Transport bifurcations have been linked to turbulence suppression mechanisms, most notably E × B shear suppression. Many theoretical studies of transport bifurcation have been reported,[2] but the high spatio-temporal resolution measurements of both gradients and turbulence needed for a careful study of these bifurcation phenomena are relatively difficult to perform on large fusion devices. Thus, a complete detailed experimental study of transport bifurcations has not been reported. In particular, the role of turbulence generated flows in internal barrier transitions has not been elucidated.

In recent experiments on the upgraded linear cylindrical plasma device, Controlled Shear Decorrelation (CSDX-U), we observed a transport bifurcation and related interesting phenomena. These occur due to the variation of the axial magnetic field B_z as a control parameter. In spite of the fact that the experiments were carried out on a linear plasma device, our results surprisingly show certain similarities to tokamak experiments. A comparison between our study and relevant tokamak results is given in Table I. As we increase B_z above a threshold ~1200 G, both the density and ion pressure profiles significantly steepen, the Reynolds stress-driven E × B flow shear sharply increases, and reductions in turbulence and particle transport are observed.[3] Thus, a transport barrier is formed, which, in many ways, resembles Internal Transport Barriers (ITBs). The work in Ref. 3 is focused on the observation and physics for the up-gradient particle flux, while this paper is focused on the formation of transport barrier at critical value of magnetic field. Above the threshold, the turbulence features change from pure drift wave (DW) (below threshold) to a mix of drift wave and ion temperature gradient (ITG). This change is reminiscent of the transition from the Linear Ohmic Confinement (LOC) regime to Saturated Ohmic Confinement (SOC) regime in tokamak devices.[4] It is believed that the LOC-SOC transition is related to a local change in turbulence mode.[5] Of particular

TABLE I. Correspondence between CSDX experiment results and confinement experiment phenomena.

Confinement experiments	CSDX experiments
$E \times B$ shear layer;	Shear layer formation;
L-H transition	particle transport bifurcation
LOC-SOC transition:	DWs/ITG fluctuation coexistence;
changes in local turbulence	changes in population with B_0
Fueling physics:	Steepening of n_0;
inward pinch; density peaking	localized up-gradient particle flux
Intrinsic rotation:	Observed intrinsic axial flow
Residual stress physics	

Note: Paper BI3 5, Bull. Am. Phys. Soc. **60**, 26 (2015).
[a)]Invited speaker.

interest is the fact that not only did we observe a reduction in particle transport, but the formation of a spatially localized region of *up-gradient* particle flux was also reported. In fact, negative, inward particle flux has also been reported in various experiments, during the application of an externally forced E × B shear flow[6] or during the L-H transition.[7,8] Last but not least, an intrinsic axial flow has been observed in CSDX, which may help better understand the intrinsic rotation related to residual stress physics.

The CSDX plasma is useful as a venue on which to study regimes of scale compression. The range of scales in the system is essential in formulating the physics model we employ. The turbulence in the usual tokamak core has a clear scale separation: $a \geq L_n > l_{meso} \gg l_{corr} > \rho$, where a denotes the plasma minor radius, L_n denotes the density gradient scale length, l_{corr} denotes the turbulent correlation length, ρ denotes the modified ion gyroradius associated with drift turbulence, and l_{meso} denotes mesoscale structures, such as E × B shear layers or avalanches. Typically in tokamaks, the normalized radius is $\rho_* = \frac{\rho}{a} \sim 10^{-3}$. In the edge transport barrier (ETB) regime found in H-mode, or in the Scrape-Off Layer (SOL), the range of scales is more compressed, so that $a \gg L_n \geq l_{corr} > \rho$. Thus in these regimes, $\rho_* = \frac{\rho}{L_n} \sim 0.1$ and the mesoscale range effectively vanishes. For these experiments on CSDX-U, the scaling is $a > L_n \sim l_{corr} \geq \rho$, where $a = 10$ cm, $L_n \sim 3$–4 cm, and $\rho \sim 1$ cm. Thus for these experiments, $\rho_* = \frac{\rho}{L_n} \sim 0.3$. It is obvious that the standard core ordering is violated on CSDX, but our experiments have a range of scales comparable to ETB or SOL regimes (i.e., no clear mesoscale range). This makes CSDX-U a promising testbed for exploring drift-wave physics in compressed scale regimes. This discussion is shown in Figure 1.

The remainder of the paper is organized as follows: Sec. II gives a detailed description of the significant changes in profiles and transport, as the magnetic field is gradually increased above the threshold; Sec. III discusses the experimental observations of particle transport bifurcation and hysteresis in density gradient; Sec. IV shows a study of locally inward turbulent particle flux related to the transport bifurcation; Sec. V gives a summary and discussion.

II. PROFILES AND TRANSPORT CHANGE FOR $B \geq B_{Cr}$

CSDX is equipped with a 13.56 MHz, 5 kW 15 cm diameter RF, radio frequency, helicon wave source using an m = 1 helical antenna. The device is operated with insulating end plates on both ends; this has been shown to eliminate radial currents flowing through endplates,[9,10] and instead the radial current is carried by ion polarization drifts or, equivalently, the turbulent Reynolds stress[11] as it occurs on closed field line regions of confinement devices. A digitizer with up to 96 channels sampling at 500 kHz and anti-aliasing filters is used to record probe data. The resulting Nyquist frequency is 250 kHz, well above the observed fluctuation frequency. An RF matching circuit is adjusted such that less than 30 W of power is observed to be reflected. Measurements of mean plasma profiles, the fluctuating density, potential, and electric fields, along with the resulting turbulent particle flux, are made by both an 18-tip Langmuir probe inserted radially in a port located 1 m downstream from the source, and a 4-tip Langmuir probe located 1.7 m downstream from the source. Details about the layouts of the two probes can be found in Refs. 12 and 13. In the absence of strong electron temperature fluctuations, the floating potential fluctuations are interpreted as plasma potential fluctuations. Similarly, the measured ion saturation current fluctuations are interpreted as density fluctuations. Both probe systems have yielded similar experimental results for profiles, particle fluxes, and Reynolds stresses. We also use a Phantom high speed camera placed at the end of the machine to capture the motion of the visible plasma light emission. The light intensity fluctuations are considered to be proportional to the ion saturation current and thus a proxy for density fluctuations.[14,15] Detailed description of the fast camera and optical layout can be found in Ref. 16. As recently discussed in detail elsewhere,[17] detailed statistical properties and dispersion relations can be determined from the fast imaging data and can be related to plasma instabilities thought to be operative in the experiment. In addition, a laser induced fluorescence (LIF) method has been employed to obtain radial profiles of the azimuthal ion fluid velocity, parallel ion flow velocity, and ion temperature. LIF measures the Doppler resolved velocity distribution functions (VDF) of argon ions, and the full width at half maxima (FWHM) of the VDF represents the average ion

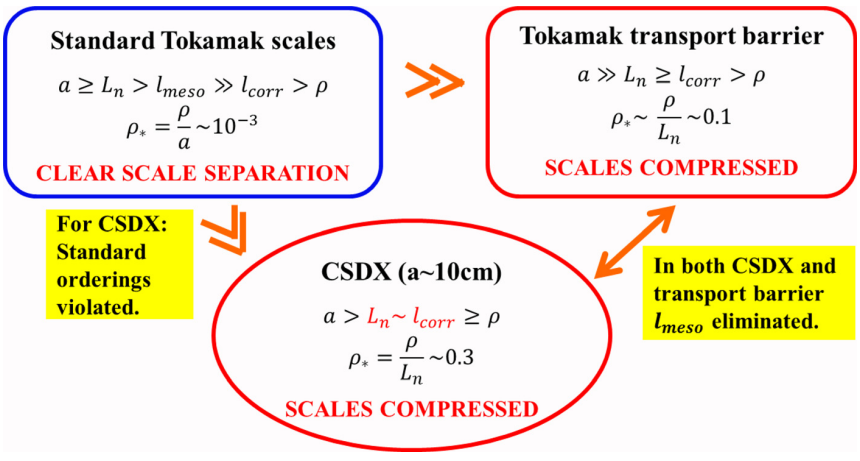

FIG. 1. Scaling comparison between standard tokamak, tokamak transport barrier regime, and CSDX.

temperature of the distribution. The shift of the peak of the distribution from a standard reference line gives the ion fluid velocity. The detailed description of LIF setup on CSDX can be found in Ref. 18.

Previous studies in CSDX[19] have demonstrated a controlled transition to a weakly turbulent state as the magnetic field is increased from ($B \sim 400$ G) to ($B \sim 1000$ G). As the magnetic field is further increased, a sharp potential gradient at the edge introduces a very strong E × B shear-driven instability. At $B \sim 1200$ G (± 100 G), a global transition to a plasma state with centrally peaked narrow density profiles, strong edge potential gradients, and a very pronounced bright, visually well-defined plasma core occurs. Details about this global transition can be found in Ref. 16. In these experiments, we undertook a careful magnetic field scan ($\Delta B = 30$G) from 800 G to 1600 G. In this paper, we focus most of our attention on two magnetic field conditions just below and just above the threshold (B = 1200 G), in order to elucidate the clear changes in profiles and fluctuations. Figures 2(a) and 2(b) show the time-averaged electron density n_0 measured by Langmuir probe and ion pressure $P_i = n_0 T_i$, respectively, where T_i was measured by LIF. A significant steepening in both mean density and ion pressure profiles has been observed at r ∼ 3.5 cm. The radial scale length of density ($L_n = |\nabla \ln n|^{-1}$) drops from 5 cm to 2 cm, also indicating a transition occurs in the radial particle transport.

The E × B drift velocity can be estimated by $V_{EXB} = V_{fluid} - V_{d,i}$, where V_{fluid} is total fluid velocity obtained from LIF measurements of the ion velocity distribution function, and $V_{d,i}$ is the ion diamagnetic velocity calculated from $V_{d,i} = \frac{\nabla(nT_i)}{enB}$. The resulting V_{EXB} profile is shown in Figure 3(a). Below the transition threshold (B = 1100 G), the flow shear is weak, while at 1300 G, a stronger velocity shear is formed at r ∼ 3.5 cm. The electron diamagnetic angular velocity $\Omega_{d,e}$, calculated from the experimentally measured electron diamagnetic velocity as $\frac{V_{d,e}}{r}$, is also a strong a function of radius, as seen in Figure 3(b). Note that as the magnetic field is increased above threshold, there is a rapid and large variation in $\Omega_{d,e}$.We show later that this rapid variation is related (by quasilinear theory) to the formation of the local negative particle flux. In order to show more robust evidence of an increase in E × B shearing, we calculated the non-dimensional shearing criterion $|v'_{E\times B}\tau_c|$ for 1100 G and 1300 G, as shown in Figure 3(c). Here, τ_c denotes the turbulent fluctuation correlation time computed from fast camera imaging data. We can see that the shearing criterion increases more than doubles as the B field changes from 1100 G to 1300 G, and begins to exceed unity. The E × B flow shearing scale length L_v, calculated to be $L_v = |\nabla \ln(v_{E\times B})|^{-1}$, decreases from 3.4 cm to 1.1 cm when we increase B field from 1100 G to 1300 G. The radial correlation length Δr_c is ∼1.3 cm at 1300 G. Thus, we find that the two length scales become comparable at 1300 G, in a regime of strong shear. The turbulent density and floating potential rms-amplitudes are also markedly reduced as B is increased above the threshold value, as shown in Figure 4.

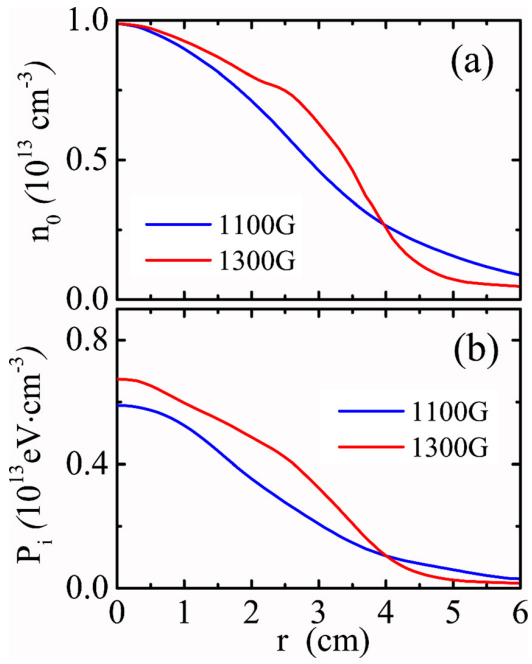

FIG. 2. Radial profiles of (a) mean density n_0, (b) mean ion pressure P_i for two different magnetic fields lying just below (1100 G) and just above (1300 G) the threshold for transport barrier formation.

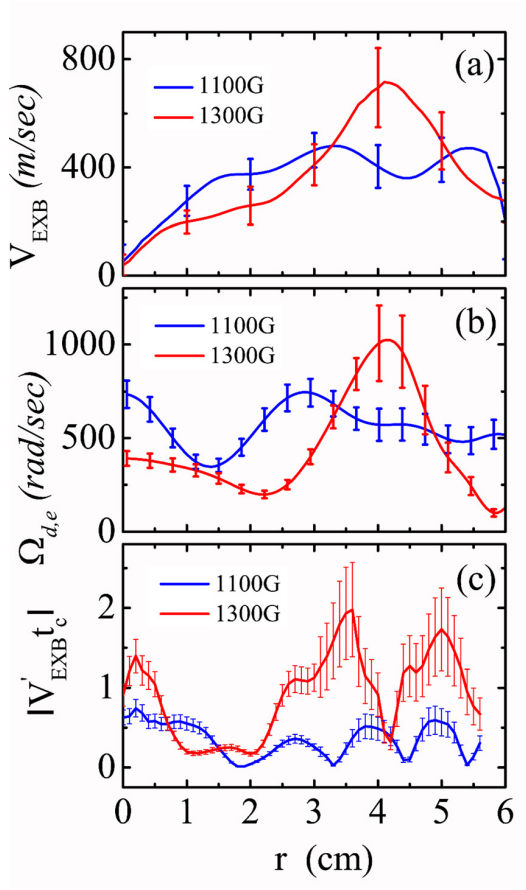

FIG. 3. Radial profile of (a) **E** × **B** drift velocity calculated from $\boldsymbol{V_{EXB}} = \boldsymbol{V_{fluid}} - \boldsymbol{V_{d,i}}$, (b) electron diamagnetic drift angular velocity, and (c) shearing criterion $|\boldsymbol{V'_{E\times B}}\tau_c|$. The **E** × **B** shearing rate and diamagnetic angular velocity both increase significantly when the magnetic field exceeds the critical value.

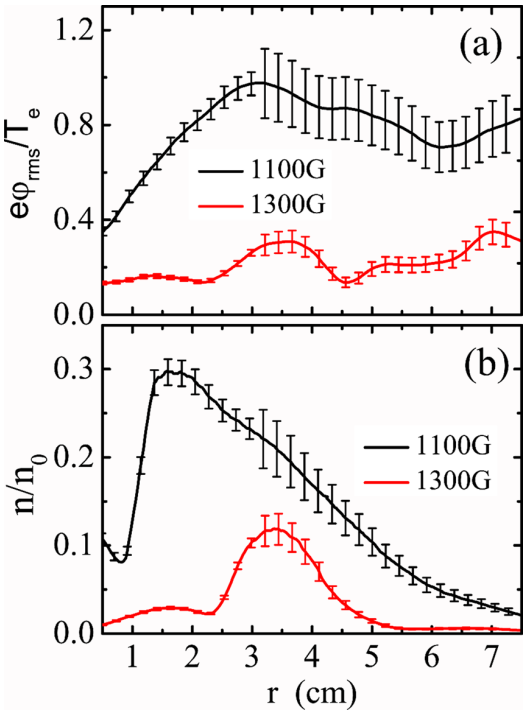

FIG. 4. Radial profiles of the standard deviations of (a) floating potential and (b) density. The floating potential has been normalized by the electron temperature T_e (4 eV)and the density by the equilibrium density n_0, both evaluated locally at 3.5 cm. A marked decrease in turbulent fluctuation amplitude occurs when the magnetic field is increased above the critical value.

Figure 5 shows the radial profiles of the axial flow velocities V_z measured by the LIF for three magnetic fields. In the parallel direction, the V_z profiles show that the inner plasma flows away from the source toward the pump end of the machine. The central axial velocity is increasing as we increase the magnetic field above the threshold 1200 G, and there is a parallel flow shear that develops at B > 1200G.

III. IS THERE A TRANSPORT BIFURCATION?

The steepening of the density and ion pressure profiles, the formation of a strong $E \times B$ flow shear, and the reduction in turbulence all occur at a critical value of magnetic field, $B_{Cr} \sim 1200$ G. These phenomena resemble those that are encountered in the development of transport barriers in toroidal confinement devices.[20,21] To further explore this similarity, as shown in Figure 6, we plot the dependence of turbulence particle flux on the absolute value of density gradient. The data were taken by increasing B field every 30 G (the minimum increment we could achieve), at fixed radius r = 3.5 cm (this is the region where the density gradient gets steepened, and strong E × B flow shear is located). Below threshold, we saw relatively linear dependence, for which a reduction in the local turbulent particle flux correlates with an increase in local density gradient (shown in red solid squares). As the B field went above threshold, a jump in the dependence occurs, and both of the local turbulent particle flux and density gradient change, by as much as 40%. This discontinuity, shown in Figure 6, suggests a transport bifurcation occurs.

Detailed observations of the density gradient evolution with changing magnetic field confirm the transport bifurcation. Figure 7 shows the forward/backward transitions with the variation of the magnetic field, plotted in blue and red curves, respectively. The density gradient evolves smoothly as we increase the magnetic field approaching the threshold. A sudden increase of density gradient occurs just above the threshold, and the density gradient again smoothly evolves with magnetic field. When the magnetic field is then decreased from high values, the gradient evolution initially retraces the behavior found during the increasing B field scan. However, the collapse of the density gradient does not occur until the magnetic field is well below the critical value found for the forward transition. Therefore, a clear hysteresis loop in the evolution of the density gradient versus magnetic field is observed. Experiments also indicate that the loop area is proportional to the RF heating power. Detailed studies of the relationship between the input power and hysteresis loop will be reported in a future work.

In a spontaneously self-organized system, sheared E × B flows are generated from ∇n-driven DW turbulence via turbulent Reynolds stress $\tilde{V}_r \tilde{V}_\theta$, as has been shown by theory,

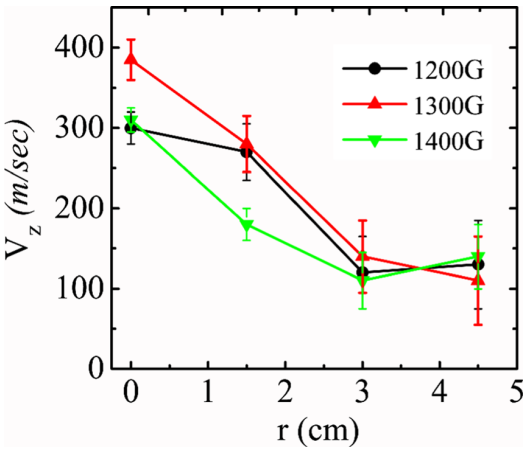

FIG. 5. Radial profile of parallel flow velocity measured by LIF for B = 1200 G, 1300 G, and 1400 G.

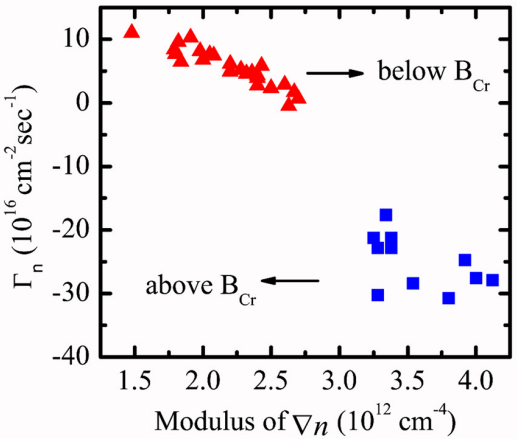

FIG. 6. Dependence of the particle flux on the value of density gradient during a magnetic field scan from 800 G to 1600 G. Data are taken at r = 3.5 cm.

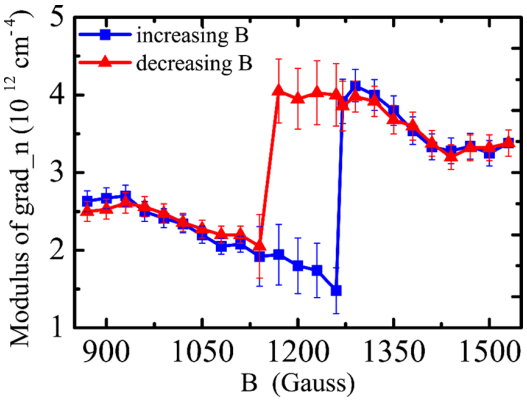

FIG. 7. Hysteresis in $\nabla \boldsymbol{n}$ is observed to occur as a function of variation of magnetic field.

simulations, and experiments.[22,23] The rate of Reynolds work, defined as the turbulence-driven Reynolds force times the E × B flow velocity $P_{Re} = -\frac{\partial \tilde{V}_r \tilde{V}_\theta}{\partial r} V_{E\times B}$, provides a measure of the power transferred from the turbulence to the $E \times B$ flow. The blue curve in Figure 8 shows the radially integrated Reynolds work, $\int_0^a r P_{Re} dr$ which denotes the total work done by the turbulence on the flow over the entire plasma cross-section. The red curve shows the normalized density gradient $1/L_n$. Here, we show results for B = 1100, 1200, 1300, and 1400 G. Above 1200 G, we find a sharp increase in the total Reynolds work that is correlated with the significant steepening of the density gradient. The increased Reynolds work can lead to an increased shear flow, which in turn can react back on the turbulence to reduce the transport.

We find that a mode propagating in the ion diamagnetic direction is excited above the threshold $\boldsymbol{B_{Cr}}$ using the density and ion pressure profiles as shown in Figure 2. We hypothesize this ion feature is ion temperature gradient (ITG) mode. This conjecture is supported by observations of the plasma density fluctuations as measured by changes in the $\mathbf{A_{rI}}$ visible light emission at 1000 G and 1400 G.[34] Figure 9(a) shows that at 1000 G, the electron drift wave fluctuation features are dominant over the whole plasma cross-section, propagating in the electron diamagnetic drift (EDD)

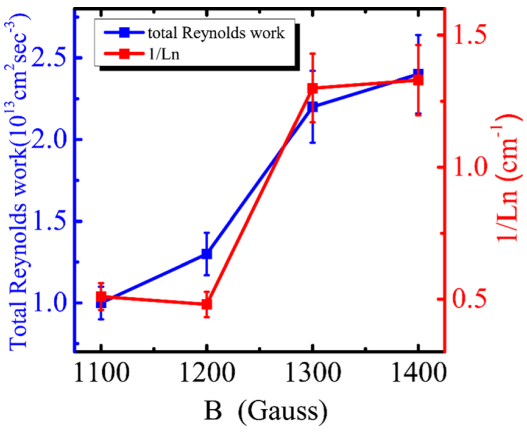

FIG. 8. Total Reynolds work and normalized density gradient $1/\mathbf{L_n}$ versus B field. The Reynolds work increases markedly at the same value of B for which the density gradient steepens.

direction. As we increase the B field to 1400 G when the ion pressure profile steepens, a fluctuation feature propagating in the ion diamagnetic drift direction (IDD) appears in the r < 2 cm region with relatively large azimuthal mode number (m ∼ 10) [shown in Fig. 9(b)]. To investigate this phenomenon, we applied a spatial Fourier transform to the imaging data at a fixed radius to obtain the conditional wavenumber-frequency spectra $\hat{\mathbf{S}}(\boldsymbol{k}_\theta, \boldsymbol{f}) = \frac{S(k_\theta, f)}{\sum_{k_\theta} S(k_\theta, f)}$. Here $\hat{\mathbf{S}}(\boldsymbol{k}_\theta, \boldsymbol{f})$ denotes the measured azimuthal mode number-frequency dispersion relation. The azimuthal mode number m is then estimated according to the expression $\mathbf{m} = \boldsymbol{k}_\theta \boldsymbol{r}$. The results are shown in Figure 10, which gives the measured dispersion relation for light intensity fluctuations at r = 3 cm for 1000 G (a) and 1400 G (b). A drift-wave like dispersion relation is observable at 1000 G. This result is similar to the previous DW-ZF study on CSDX.[24] However, at 1400 G, we observe the spectra developed in ion mode region along with the usual DW turbulence. Note that even though the ion feature appears above threshold, the primary turbulence is still DW turbulence.

These changes in turbulence also result in a significant change in global particle balance that would be expected to accompany steepened plasma radial profiles. CSDX is an open plasma device into which we radially inject argon gas at a constant flow rate of 25 sccm. The particle loss is due to turbulent radial transport, classical cross-field (radial) transport, and end loss. The time scale for particle loss τ is estimated from the ratio of the integrated flux through the corresponding surface areas and the total number of particles within the volume. To get the total number of particles in our system, we took $n_0(r)$ and did a volume integral over length of CSDX (∼300 cm) and radius of 4 cm. To estimate the integrated parallel particle flux, we integrated the mean parallel flux $n_0(r)V_{\|}(r)$ over the surface area at the end of the machine, for radius = 4 cm. To get the surface integrated radial flux, we used the turbulent particle flux that is measured from the probes and do a surface integral over the curved surface of the cylinder at r = 4 cm and the length of CSDX. We also compared to the classical transport rate by Braginski.[25] The results are shown in Table II below. We see that, for $B < B_{Cr}$, the particle losses are dominated by the radial transport caused by turbulence. When $B > B_{Cr}$, the radial turbulent transport is drastically reduced, and particle losses are now due to a combination of parallel transport and classical cross-field (i.e., collisional) transport. As a result, a steepening of the radial plasma density will naturally occur. This will, in turn, lead to an increase in collisional heating of the ion fluid, which will result in higher central ion temperatures. As a result, we see the steepening of both density and ion temperature in the experiment [Fig. 2]. If the T_i gradient becomes strong enough, this then sets up the conditions for the onset of an ITG mode[26,27] that will coexist with the collisional drift waves, which will regulate ∇T_i. We conjecture that this scenario is what explains the appearance of the ion feature, discussed above.

Figure 11 presents a flowchart that shows the main elements involved in the formation of a transport barrier, namely, finite Reynolds work, sheared E × B flow, and their

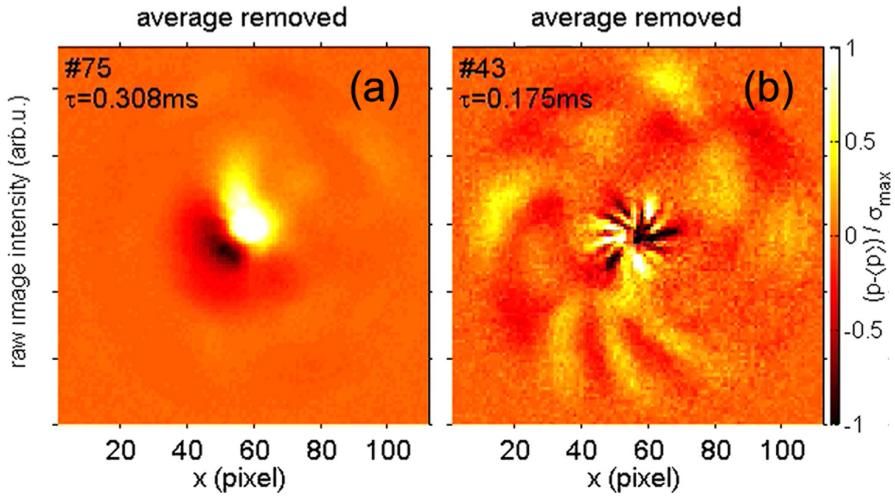

FIG. 9. Fluctuation feature observed from light emission of neutral argon emission ($\mathbf{A_{rI}}$). (a) B = 1000 G and (b) B = 1400 G.

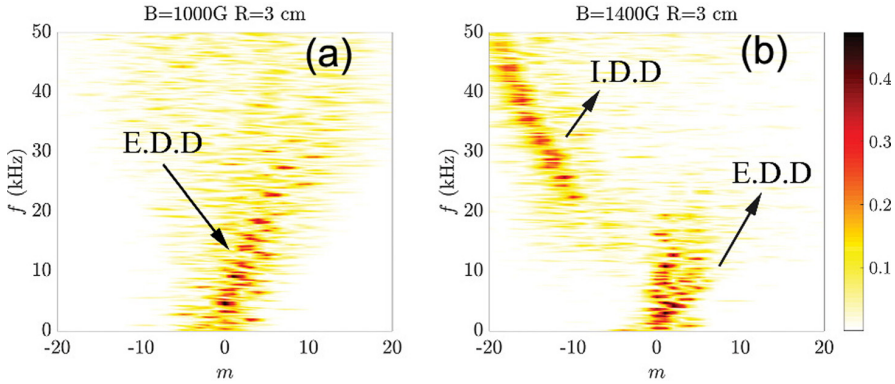

FIG. 10. Conditional spectra of light intensity fluctuation $\hat{\mathbf{S}}(\boldsymbol{m},\boldsymbol{f})$ at r = 3 cm for (a) B = 1000 G and (b) B = 1400 G.

impact on turbulence, transport, and the resulting profiles. This provides a summary of the observations. The process of transport barrier formation is initiated when we gradually increase the magnetic field above a threshold ∼1200 G, which results in a global transition, signified by a sudden increase in density and ion pressure gradients. The increasing turbulent Reynolds stress leads to a strong E × B flow shear. As a result of the resulting strong shear, a reduction in both turbulence and particle transport occurs. Since turbulent cross-field transport is, initially, the dominant transport mechanism, its reduction leads to the formation of a steepened density gradient.

IV. STUDY OF LOCALLY INWARD TURBULENT PARTICLE FLUX

In addition to a self-sustained axial flow absent momentum input [Fig. 5] and the co-existence of ion and electron features [Fig. 10], another interesting phenomenon that occurs above threshold B_{Cr} is the locally inward turbulent particle flux.[3] We notice that the region of locally inward particle flux is comparable to radial turbulence correlation length scale ∼1 cm. Thus, while we tried to interpret this phenomenon by using quasilinear approaches, we note here that caution is required in applying such methods to a state where the requisite scale separation is not realized. In Figure 6, we can see that this locally inward particle flux correlates with the transport bifurcation. We undertook different theoretical approaches to explain the locally inward flux. For ∇n-driven resistive drift turbulence, the sign of turbulent particle flux Γ_n is determined by the competition between the local value of $\omega_{d,e}(r)$ and ω_r,[28] where $\omega_{d,e} = k_y v_{d,e} = \Omega_{d,e} m$ is the local diamagnetic frequency, and ω_r is the eigenfrequency of the global drift-wave mode (not the mode growth rate).[29] In our experiments, the angular frequency $\Omega_{d,e}$ varies in radius, shown in Figure 3(b), resulting in a $\omega_{d,e}$

TABLE II. Comparison of particle loss due to radial turbulent transport, parallel transport, and classic transport for the conditions that B is below and above threshold.

B(G) \ (s^{-1})	$1/\tau_\perp$	$1/\tau_\parallel$	$1/\tau_{classic}$
1000	714	65	22
1300	35	106	28

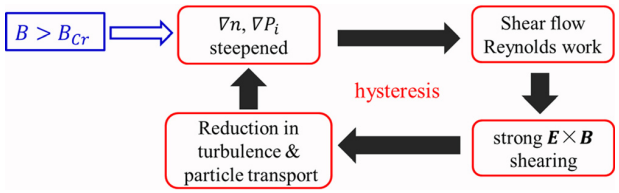

FIG. 11. Partial summary of transport bifurcation and hysteresis-related observations.

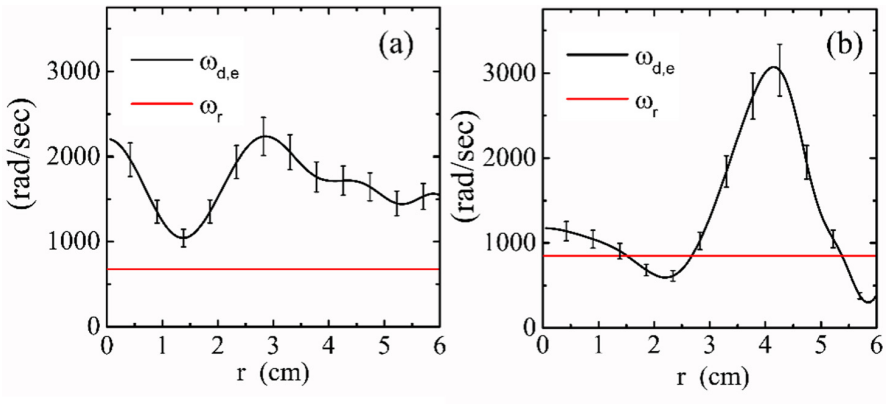

FIG. 12. Comparison between local diamagnetic frequency $\omega_{d,e}$ and drift wave frequency ω_r for B = 1000 G (a) and 1300 G (b).

variation as a function of radius. Because the radius is not so large compared the fluctuation radial scale length, and also due to the lack of magnetic shear, the drift eigenmodes tend to fill the entire plasma cross-section (i.e., they are "global modes") even while $\omega_{d,e}(r)$ varies rapidly. In Figure. 12, we plot $\omega_{d,e}(r)$ from experiment measurement and ω_r obtained from a linear instability calculation. For B = 1000 G (below threshold), ω_r is less than $\omega_{d,e}$ at all radii, where Γ_n is positive, indicating outward particle transport. In contrast, for B = 1300 G, the rapid and large variation in $\omega_{d,e}$ leads to a drop below ω_r in a limited spatial region, which results in a quasilinear locally inward particle flux. And for cases where there is a local net inward flux, the *radially integrated particle flux is always outward*, which is consistent with ∇n-driven resistive drift turbulence. The condition and location where the local inward particle flux appears in a quasilinear theory calculation is similar to where it appears in the measured particle flux.[3] The physics origin of the sharp variation in $\omega_{d,e}$ is not well understood. We conjecture it is due to the strong E × B shear, which is radially co-located. More generally, it is not clear that how a drift wave-driven system can configure itself to drive a locally up-gradient flux by a global density relaxation.

We also examined other possible candidates for causing the inward particle flux. Based on a simple Hasegawa-Wakatani model with both a turbulent-stress driven flow shear and a background density gradient, both axially symmetric ($k_{\|} = 0$) and non-axially symmetric ($k_{\|} \neq 0$) shear flow instabilities can be driven ($k_{\|}$ is the axial mode number).[28] By using our experimental profiles in a quasilinear expression for the local particle flux, we find that the particle transport driven by standard KH modes ($k_{\|} = 0$) is always outward. Drift-KH mode can drive a pinch, but this inward particle pinch is not sufficient to locally overcome the relaxation-driven diffusive outward flux. We also considered an ion-mixing mode-driven pinch. Coppi and Spight have worked out that the ITG modes along with non-adiabatic electron response can produce a particle pinch. This is the ion-mixing mode (IMM) mechanism.[30] Due to the observation of a steepening in density gradient, along with a peaking in ion temperature [Fig. 2], another possible candidate for explaining the inward particle flux is IMM mechanism. But for the IMM to drive a net inward particle flux requires that the electron temperature gradient should exceed a threshold of $\eta_e > 2/3$. However, the measurement for T_e shows that in the region where we observed a net inward particle flux, the $\nabla T_e \sim 0$. Thus, the criterion for IMM-driven inward particle flux is not satisfied. Finally, Kosuga *et al.*[31] have proposed that the parallel shear flow instability (PSFI) with non-adiabatic electrons may drive inward flux. This mechanism is similar to the IMM. However, simple estimates indicate that CSDX axial flows are far below threshold for the PSFI, so this mechanism is not viable here.

V. DISCUSSION AND CONCLUSIONS

In this paper, we have showed that particle transport bifurcation and hysteresis occur spontaneously above a threshold B_{Cr} in a linear plasma system. These are seen to be correlated with the following observations: steepening of density and ion pressure gradients, reinforced E × B shearing, and reduction in turbulence and particle transport, increased Reynolds work, and changes in turbulence from DWs to a mix of DWs and ITGs. Also, a localized regime of inward particle flux occurs above threshold too. Figure 13 presents a flowchart containing two feedback loops that provides a qualitative summary of the changes we observe in the self-organization of the drift-wave turbulence. The loop that contains red boxes shows the process related to the formation of transport bifurcation, as shown in Figure 11. The blue boxes denote the feedback of the profile evolution on the underlying instability, the quasilinear particle flux, and the development of a locally inward particle flux, which acts to further modulate the background gradients. The locally steepened density gradient gives rise to a rapid variation in $\Omega_{d,e}$ at r ~ 2–3 cm. When the local value $\Omega_{d,e}$ drops below

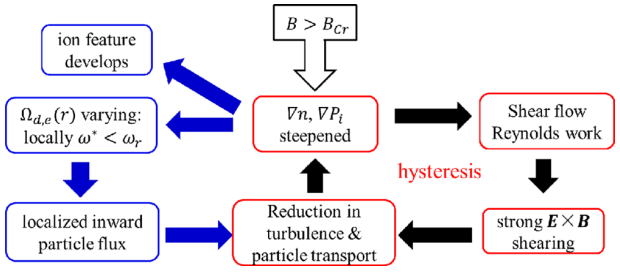

FIG. 13. Flowchart of spontaneous profile self-organization in drift-wave turbulence.

ω_r/m, an localized inward particle flux appears that leads to further steepening of the density gradient. Increased central plasma density leads to increased collisional ion heating, which results in a steepening in ion pressure that leads to the onset of ITG fluctuations, consistent with the ion feature seen from fast camera.

Several questions remain. First of all, what are the trigger mechanism and criterion for transition? It is a puzzle that all of the interesting physics phenomena appear above the threshold 1200 G. What is the dimensionless physics parameter which underlies this value of B_z? In a spontaneous realization of DW-ZF system, the competition between turbulence-driven transport and shear flow is thought to play an essential role; that is, the energy released from density gradient and the energy transferred into flow compete. Does this set the critical B? Second, what is the underlying physics for the transport bifurcation? The most likely candidate is the turbulent Reynolds stress-driven flow. We saw in Figure 8 that the sharp increase in density gradient is correlated with a sharp increase in the Reynolds work. And the correlation between Reynolds-stress driven flow shearing rate and inward particle flux given in Ref. 3 shows that a transient increase in the local azimuthal shearing rate leads the subsequent increase in the up-gradient particle flux. It is therefore reasonable to expect that an increase in the Reynolds stress may lead an increase in the density gradient. However, time-evolution experiments on the forward/back transition are needed in order to probe the trigger mechanism and criterion for transition. Note that the physics of the flow in CSDX is fundamentally different from the core of a tokamak since, on the one hand, there is no scale-invariant drag (viscosity only acts as damping), but, on the other hand, the absence of magnetic shear enables onset of shear flow instability. Finally, it is interesting to note what aspects of this story are new to CSDX and are not only revisitations of phenomena well known from tokamak ITB experiments. This includes: (i) the observation of a peaked profiles, strong shear state achieved with edge fueling and no additional heating. We do note that the IOC (Improved Ohmic Confinement) state of ASDEX[32] and the PITB (Particle ITB) state of HL-2A[33] have same features in common with the result reported here: (ii) the clearest and well-demonstrated hysteresis loop related to the transition; (iii) the measurements of core plasma Reynolds stresses and the demonstration of the link between the fluctuation Reynolds work and the barrier transition; (iv) the clear observation of electron and ion feature co-existence in the core plasma, as ∇T_i steepens. Further comparisons and contrasts with tokamaks will be reported in the future.

ACKNOWLEDGMENTS

This research was supported by the U.S. Department of Energy Grant under Award Nos. DE-FG02-07ER54912, DE-FG02-04ER54738, and DE-SC0008378. We thank J. Mckee, S. Sears, and E. E. Scime from West Virginia University for their assistance with LIF diagnostics. We thank J. Li, Y. Kosuga, O. Gurcan, P. Vaezi, and R. Hajjar for useful discussions. One of the authors (L. Cui) acknowledges useful discussions with W. Solomon and R. Nazikian.

[1]G. D. Conway, C. Angioni, R. Dux, F. Ryter, A. G. Peeters, J. Schirmer, C. Troester, and C. F. N. R. Group, Nucl. Fusion **46**, S799 (2006).
[2]V. B. Lebedev and P. H. Diamond, Phys. Plasmas **4**, 1087 (1997).
[3]L. Cui, G. R. Tynan, P. H. Diamond, S. C. Thakur, and C. Brandt, Phys. Plasmas **22**, 050704 (2015).
[4]C. L. Rettig, T. L. Rhodes, J. N. Leboeuf, W. A. Peebles, E. J. Doyle, G. M. Staebler, K. H. Burrell, and R. A. Moyer, Phys. Plasmas **8**, 2232 (2001).
[5]J. E. Rice, M. J. Greenwald, Y. A. Podpaly, M. L. Reinke, P. H. Diamond, J. W. Hughes, N. T. Howard, Y. Ma, I. Cziegler, B. P. Duval *et al.*, Phys. Plasmas **19**, 056106 (2012).
[6]T. A. Carter and J. E. Maggs, Phys. Plasmas **16**, 012304 (2009).
[7]G. R. Tynan, J. A. Boedo, D. S. Gray, R. Van Nieuwenhove, G. Van Oost, and R. R. Weynants, J. Nucl. Mater. **196–198**, 770 (1992).
[8]S. H. Muller, J. A. Boedo, K. H. Burrell, J. S. deGrassie, R. A. Moyer, D. L. Rudakov, W. M. Solomon, and G. R. Tynan, Phys. Plasmas **18**, 072504 (2011).
[9]S. C. Thakur, M. Xu, P. Manz, N. Fedorczak, C. Holland, and G. R. Tynan, Phys. Plasmas **20**, 012304 (2013).
[10]D. A. Russell, J. R. Myra, and D. A. D'Ippolito, Phys Plasmas **16**, 122304 (2009).
[11]P. H. Diamond and Y. B. Kim, Phys. Fluids B **3**, 1626 (1991).
[12]Z. Yan, J. H. Yu, C. Holland, M. Xu, S. H. Muller, and G. R. Tynan, Phys. Plasmas **15**, 092309 (2008).
[13]M. Xu, G. R. Tynan, C. Holland, Z. Yan, S. H. Muller, and J. H. Yu, Phys. Plasmas **16**, 042312 (2009).
[14]G. Y. Antar, J. H. Yu, and G. Tynan, Phys. Plasmas **14**, 022301 (2007).
[15]S. Oldenburger, C. Brandt, F. Brochard, N. Lemoine, and G. Bonhomme, Rev. Sci. Instrum **81**, 063505 (2010).
[16]S. C. Thakur, C. Brandt, L. Cui, J. J. Gosselin, A. D. Light, and G. R. Tynan, Plasma Sources Sci Technol. **23**(4), 044006 (2014).
[17]A. D. Light, S. C. Thakur, C. Brandt, Y. Sechrest, G. R. Tynan, and T. Munsat, Phys. Plasmas **20**, 082120 (2013).
[18]S. C. Thakur, D. McCarren, T. Lee, N. Fedorczak, P. Manz, E. E. Scime, G. R. Tynan, and M. Xu, Phys. Plasmas **19**, 082102 (2012).
[19]M. J. Burin, G. R. Tynan, G. Y. Antar, N. A. Crocker, and C. Holland, Phys. Plasmas **12**, 052320 (2005).
[20]P. W. Terry, Rev. Mod. Phys. **72**, 109 (2000).
[21]F. Wagner, Plasma Phys. Controlled Fusion **49**, B1 (2007).
[22]G. R. Tynan, A. Fujisawa, and G. McKee, Plasma Phys. Controlled Fusion **51**(11), 113001 (2009).
[23]P. H. Diamond, S. I. Itoh, K. Itoh, and T. S. Hahm, Plasma Phys. Controlled Fusion **47**, R35 (2005).
[24]M. Xu, G. R. Tynan, C. Holland, Z. Yan, S. H. Muller, and J. H. Yu, Phys. Plasmas **17**, 032311 (2010).
[25]S. I. Braginskii, "Transport processes in a plasma," Rev. Plasma Phys. **1**, 205–311 (1965).
[26]A. K. Sen, B. Song, and J. Chen, Phys. Scr. **52**, 467 (1995).
[27]R. G. Greaves, J. Chen, and A. K. Sen, Plasma Phys. Controlled Fusion **34**, 1253 (1992).
[28]A. Ashourvan, P. H. Diamond, and O. D. Gurcan, Phys. Plasmas **23**, 022309 (2016).
[29]P. H. Diamond, A. Hasegawa, and K. Mima, Plasma Phys. Controlled Fusion **53**(12), 124001 (2011).
[30]B. Coppi and C. Spight, Phys. Rev. Lett. **41**, 551 (1978).
[31]Y. Kosuga, S. Itoh, and K. Itoh, Plasma Fusion Res. **10**, 3401024 (2015).
[32]F. Wagner, G. Becker, K. Behringer, D. Campbell, A. Eberhagen, W. Engelhardt, G. Fussmann, O. Gehre, J. Gernhardt, G. V. Gierke *et al.*, Phys. Rev. Lett. **49**, 1408 (1982).
[33]Y. Liu, Z. B. Shi, Y. B. Dong, H. J. Sun, A. P. Sun, Y. G. Li, Z. W. Xia, W. Li, X. T. Ding, W. W. Xiao *et al.*, Phys. Rev. E **84**, 016403 (2011).
[34]See supplementary material at http://dx.doi.org/10.1063/1.4944819 for camera movies recording light of Ar I emission lines for two different magnetic fields B = 1000 G and 1400 G.